23rd International Conference on Material Forming (ESAFORM 2020)

A Modified Hockett-Sherby Law Enabling the Description of the Thermomechanical Behaviour of the AA6061-T6

Marta C. Oliveira[a],*, Lisa Germain[b], Hervé Laurent[b], Vasco M. Simões[a], Diogo M. Neto[a], José L. Alves[c], Luís F. Menezes[a]

[a]CEMMPRE, Department of Mechanical Engineering, University of Coimbra, Pólo II, Rua Luís Reis Santos, Pinhal de Marrocos, 3030-788 Coimbra, Portugal
[b]Univ. Bretagne Sud, UMR CNRS 6027, IRDL, F-56100 Lorient, France
[c]CMEMS, Department of Mechanical Engineering, University of Minho, Campus de Azurém, 4800-058 Guimarães, Portugal

* Corresponding author. Tel.: +351-239-790-700; fax: +351-239-790-701. E-mail address: marta.oliveira@dem.uc.pt

Abstract

The use of warm temperatures in the forming process enhances the aluminium alloys formability and reduces the springback effect, when compared with room temperature conditions. However, in order to be able to design warm forming processes it is necessary to describe the influence of temperature and strain rate on the mechanical behaviour of the material. This work presents the procedure adopted to identify the parameters of a thermomechanical Hockett-Sherby type law, for the EN AW 6061-T6 aluminium alloy, based on previously reported results from experimental uniaxial tensile tests performed on a Gleeble machine [1]. The experimental data were analysed, in order to obtain the true stress-plastic strain curves, for a temperature range between room temperature and 200°C, at three different strain rates. A classical identification procedure was applied to identify the parameters of a modified Hockett-Sherby type law, which describes the dependence of the initial yield stress on temperature. A multi-step procedure is proposed, in combination with a gradient-based method, in order to enable the selection of an initial solution prone to lead to a feasible set of parameters. The identified parameters were used to perform the numerical analysis of the uniaxial tensile tests, taking into account the non-isothermal conditions, which occur in the Gleeble device. The analysis of these tests highlights that the non-isothermal conditions promote the increase of the strain rate in the centre of the specimen. However, the presence of the strain rate gradient along the specimen length seems to have a small impact in the classical analysis of the experimental data, as long as it is based on an effective gauge length that presents a uniform deformation.

Keywords: Thermomechanical testing; Gleeble uniaxial tensile test; Hardening law; Thermomechanical hardening law; Finite element method

1. Introduction

The continuous demand to improve fuel efficiency and reduce CO_2 emissions, while increasing passenger safety standards, are imposing new challenges for car manufacturers [2]. In the context of vehicles' body structures, conventional mild steels are increasingly being replaced by lightweight materials, such as magnesium alloys, high strength steels or aluminium alloys. However, materials with a higher strength-to-weight ratio also present poor formability at room temperature, disabling the forming of panel components with complex geometries. The formability can be greatly improved by resorting to warm/hot forming processes [2–4].

The virtual design of this kind of processes demands the characterization of the constitutive properties of the material, which typically consist of the temperature- and strain rate-dependent stress-strain response, as well as the characterization of the anisotropy [5]. These properties can be obtained from the uniaxial tensile test, for which standards have been established, applicable under isothermal conditions or within a small permitted temperature deviation within the gauge length region of a specimen. The industrial application

of warm/hot forming processes demands rapid heating, which should be replicated in the uniaxial tensile tests performed. This disables the conventional use of ovens or furnaces [6]. On the other hand, the Gleeble thermomechanical testing system uses a direct resistance heating system, enabling the combination of an accurate high heating rate with the mechanical loading, possibly in a vacuum environment. Thus, it has become a standard device for this type of testing, although it is known that thermal gradients will occur in the specimen. These thermal gradients are dependent on the sample geometry and can cause its heterogeneous deformation, due to the temperature-dependent flow properties [7].

Some authors have developed a new grip design for the Gleeble device, in order to achieve uniform temperature within the effective gauge length. The comparison of the stress-strain curve obtained using the conventional and these new grips indicates that the occurrence of localized deformation with the conventional grips results in a higher strain rate level, i.e. in a higher stress level for a material showing positive strain rate sensitivity [2]. However, this comparison is performed considering a similar effective gauge length for both cases, while other authors point out that the measured stress–strain relationship is heavily affected by the definition of gauge length of the specimen [6]. In this context, the use of in situ Digital Image Correlation (DIC) systems for results analysis becomes fundamental. It can enable the definition of an effective gauge length, for which the deformation can be considered uniform before the onset of necking [3] or it can be used to measure the instantaneous cross-sectional area, necessary to evaluate the true stress-strain curve [5]. In fact, it is important to notice that it can be difficult to eliminate the temperature gradient along the cross section due to the heat loss from the clamped ends of the specimen, during the resistance heating [6]. Thus, it is important to evaluate the influence of the thermal gradient in the results analysis.

In this work, the parameters of a thermomechanical Hockett-Sherby type law are identified, for the 6061-T6 aluminium alloy, based on previously reported results from experimental uniaxial tensile tests performed on a Gleeble machine [1]. The classical identification procedure adopted uses the stress-strain curves evaluated considering an effective gauge length, determined based on the uniform deformation region, before the onset of necking. The identified parameters were used to perform the numerical analysis of the uniaxial tensile tests, taking into account the surface temperature distribution induced by the Gleeble device. The aim is to improve the knowledge concerning the influence of the temperature gradient in the analysis of the strain and strain rate measurements, as well as on the stress state that occurs in the specimen centre.

2. Experimental results analysis

To analyse the thermo-mechanical behaviour of the material it is necessary to perform experimental tests within the temperature range. In the studies conducted by Simões et al. [1,8], uniaxial tensile tests were performed under non-

isothermal conditions using a Gleeble machine. The identification of the thermo-mechanical hardening law is performed considering these results, which are detailed in the following section.

2.1. Material: 6061-T6 aluminium alloy

The 6061-T6 aluminium alloy selected for this study is commonly used for structural components in the automotive industry. The T6 heat treatment is called artificial aging since it involves solution heat treated, rapid quenching, followed by artificial aging. This alloy was selected because the T6 condition minimizes the occurrence of microstructural changes under warm conditions, at least for relatively small heat-holding times. The main alloying elements are Mg and Si, which promote precipitation hardening. The thickness of the blank was measured in several locations leading to an average value of 0.98 mm [1,8]. This value is approximately equal to 1 mm, which is the reference used by the supplier.

2.2. Non-isothermal uniaxial tensile tests

In the Gleeble device, the specimen is fixed by two copper grips and one thermocouple is welded in its centre to control the temperature, since it will extract the temperature in real time throughout the test. The contact with the cooled grips induces a thermal gradient in the specimen, which follows a polynomial distribution of degree two [9]. Therefore, a DIC system was used to evaluate the heterogeneous strain fields, in particular the major and minor strains. The system used was GOM-Aramis 3D (for further details, please refer to [1,8]).

To evaluate the true stress it is necessary to assume a uniaxial stress state, which implies a homogeneous deformation of the gauge area. Therefore, a small measurement area (total length of 3 mm and width of 10 mm) was selected at the centre of the specimen, to try to obtain a homogeneous strain field [1,8,9]. Moreover, the true stress was calculated using the results attained only until the maximum force, as in [10].

Uniaxial tensile tests were performed with the specimen oriented along the rolling direction (RD), at different temperatures (22ºC, 100ºC, 150ºC and 200ºC), where 22ºC corresponds to the room temperature (RT). For RT and 200ºC the tests were performed for three initial strain rate values: $0.0002 s^{-1}$, $0.002 s^{-1}$ and $0.02 s^{-1}$, which will be labelled v01, v1 and v10. For the other temperatures, the data is only available for a strain rate of $0.002 s^{-1}$. The velocity imposed to the grips controls the test and that is why the values presented can only be considered as initial ones. Finally, it should be mentioned that tests were also used to extract the Lankford values, at 0°, 45° and 90° to RD, as a function of temperature [8]. However, it was decided to perform the identification of the hardening law considering only the tests performed at RD.

The reproducibility of the results was verified [1,8,9] and the true stress-strain curves were analysed in order to determine the A_{gt} (percentage of total elongation at maximum force) value for each one. For some tests, there was some difference in the A_{gt} value. In those cases, the selected data always corresponds to the stress-strain curve with the highest

one. To obtain the hardening law, the stress-strain curves were treated to remove the elastic part. Figure 1 presents the stress-strain curves selected. The label adopted corresponds to the test temperature. The strain rate value is denoted with a different type of line. The same approach will be followed throughout this work. This figure shows that when the temperature increases: i) the initial yield stress decreases; ii) the difference between the initial yield stress and the maximum stress decreases, i.e. the slope of the hardening curve decreases; iii) for RT, the yield stress evolution is similar for the three strain rates, whereas, for 200ºC there is a positive strain rate sensitivity.
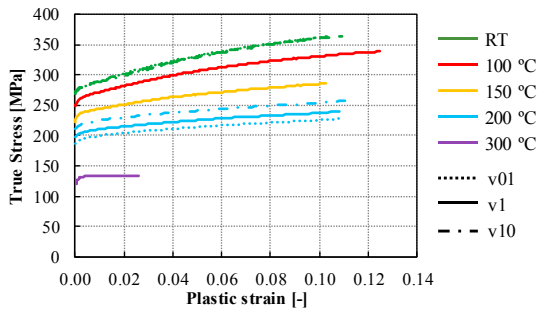

Fig. 1. Experimental stress-strain curves obtained from tensile tests performed with the specimen oriented along the RD.

3. Classical identification of the hardening law parameters

Classical identification methodologies for the hardening law parameters are developed based on the knowledge of the experimental stress-strain curve. Thus, the goal is to determine the hardening law parameters that minimize the difference between the yield stresses determined experimentally and the ones given by the hardening law selected, for all strain values.

3.1. Modified Hockett-Sherby hardening law

In order to describe the work hardening of aluminium alloys it is normally recommended to use a phenomenological Hockett-Sherby type law, to enable the description of the saturation behaviour (see Figure 1). To include the strain rate dependency it is common to introduce a power law, as proposed by Wagoner et al. [11] and previously done, for example in [12]. Thus, the yield stress, σ_y, evolves with temperature, T, and strain rate, $\dot{\varepsilon}$, as follows:

$$\sigma_y(T,\dot{\varepsilon}) = \left[\sigma_0 + Q\left(1 - \exp\left(-b\left(\bar{\varepsilon}^p\right)^n\right)\right)\right]\left[\frac{\dot{\varepsilon}}{\dot{\varepsilon}_0}\right]^m \tag{1}$$

where $\bar{\varepsilon}^p$ is the equivalent plastic strain, σ_0 is the initial yield stress, Q is the maximum change in size of the yield surface, b denotes the growth rate of the yield surface (or the hardening), n is strain hardening coefficient, $\dot{\varepsilon}_0$ is a constant strain rate normalisation factor and m is the strain rate sensitivity coefficient.

The temperature dependence was modelled by taking Q, b, n and m to be functions of temperature. The strain rate

sensitivity index m evolves exponentially with the temperature as follows:

$$m(T) = m_0 \exp\left(m_1 \frac{T}{T_m}\right) \tag{2}$$

where m_0 and m_1 are material parameters and T_m is the material melting temperature, which can be assumed to be equal to 600ºC for aluminium alloys. The strain-hardening index n was assumed to evolve linearly with temperature:

$$n(T) = n_0 - n_1\left(\frac{T}{T_m}\right) \tag{3}$$

where n_0 and n_1 are material parameters. The evolution of the size of the yield surface with the temperature is given by the following equation:

$$Q(T) = Q_0 + a_1\left[1 - \exp\left(a_2 \frac{T}{T_m}\right)\right] \tag{4}$$

where Q_0, a_1 and a_2 are material parameters.

In the original formulation of the hardening law, it is assumed that σ_0 is constant (see Eq. (1)). However, as shown in Figure 1, this assumption is not valid for the 6061-T6 alloy. Therefore, a quadratic evolution was considered:

$$\sigma_0(T) = \sigma_0 - s_1\left(\frac{T}{T_m}\right) - s_2\left(\frac{T}{T_m}\right)^2 \tag{5}$$

where σ_0, s_1 and s_2 are material parameters. Thus, the identification procedure needs to take into account a total of 12 parameters: $\dot{\varepsilon}_0$, b, m_0, m_1, n_0, n_1, Q_0, a_1, a_2, σ_0, s_1 and s_2.

3.2. Identification Procedure

An objective function was defined for each test conditions, as follows:

$$f_{itest} = \frac{1}{npoint}\sum_{i=1}^{npoint}\left(\sigma_y^{exp} - \sigma_y^{num}\right)^2 \tag{6}$$

where σ_y^{exp} and σ_y^{num} are the yield stress determined experimentally and the ones given by the hardening law, respectively. *npoint* is the number of strain values acquired of each test. Although some authors recommend the use of relative error in order to guarantee that all tests have equal opportunities to be optimised and that different units or scales should not affect the overall performance of the process [13], this option was not taken into account in this work. Moreover, equal weights were assigned to each test, such that the objective function is defined as follows:

$$f_{obj} = \sum_{itest=1}^{ntest} f_{itest} = \sum_{RT}^{200^{\circ}C} \sum_{v01}^{v10} f_{itest} \qquad (7)$$

Since there is an analytical expression for the hardening law, it was decided to resort to a Generalized Reduced Gradient (GRG) algorithm, to solve the minimization problem defined in Eq. (7). However, it is known that this type of algorithm is sensitive to the initial solution. Therefore, an iterative procedure, involving two-steps, is proposed, to guide the method towards feasible parameters.

The proposed procedure starts with the evaluation of a value for $\dot{\varepsilon}_0$ (see Eq. (1)). It is known that this constant should be lower than $0.0002 s^{-1}$, since this corresponds to the lowest value assumed in the experimental tests. Therefore, the range considered in this study was $\dot{\varepsilon}_0 \in \left[10^{-5}; 2 \times 10^{-4} \right]$ s^{-1}, which corresponds to a constraint in the optimization problem. To start the multi-step procedure, it was assumed that $\dot{\varepsilon}_0 = 2 \times 10^{-4}$ s^{-1}. Then, the following procedure was applied:

- First Step: The analysis considers only the initial yield stress values. The values extracted from the experimental tests are plotted in function of temperature and a quadratic fit is performed. The values obtained from the quadratic fit for the parameters σ_0, s_1 and s_2 are used as initial solutions to minimize the error between the experimental and numerical initial yield stress values, taking also into account the strain rate dependency. This allows the identification of an initial solution for the parameters m_0 and m_1, assuming that $\dot{\varepsilon}_0$ is known.
- Second Step: Make a first identification of the remaining parameters, followed by an optimization of all parameters, including $\dot{\varepsilon}_0$. This can result in the updating of this parameter, meaning that the First Step should be repeated. The loop between Step 1 and Step 2 ends when the value of $\dot{\varepsilon}_0$ does not change its order of magnitude.
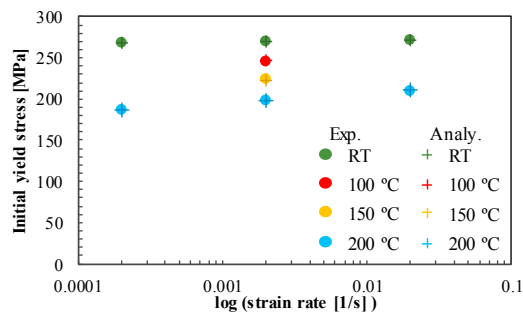

Fig. 2. Comparison between analytical and experimental initial yield stress values, as a function of the logarithm of the strain rate, with the parameters obtained in the First Step.

Figure 2 compares the analytical and experimental initial yield stress values, as obtained at the end of the First Step. This highlights the importance of using this approach to guide the optimization algorithm. Figure 3 compares the analytical and experimental yield stress curves, as obtained at the end of the Second Step, showing that the adoption of a quadratic function for the evolution of the initial yield stress enables an

acceptable description of the material behaviour. Table 1 presents the identified hardening law parameters.
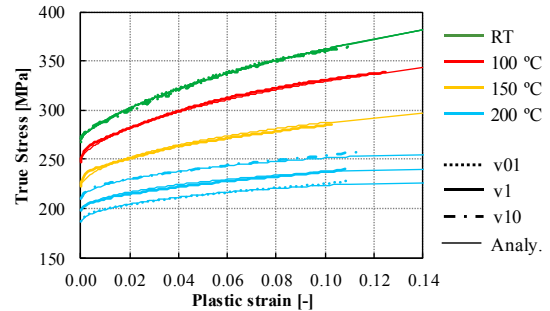

Fig. 3. Comparison between experimental and analytical stress-strain curves.

Table 1. Modified Hockett-Sherby hardening law parameters.

Parameter	Value	Parameter	Value
$\dot{\varepsilon}_0$	1.0×10^{-4} s^{-1}	σ_0	272.1 MPa
s_1	0.0 MPa	s_2	795.3 MPa
n_0	0.80	n_1	0.63
m_0	4.3×10^{-6}	m_1	26.1
b	3.2	Q_0	230.3 MPa
a_1	116.4 MPa	a_2	2.7

4. Finite element model of the Gleeble testing system

The Gleeble testing system heats the specimen by direct resistance using an electrical control scheme, which changes the applied current intensity to achieve the target temperature in the centre of the specimen, measured with a thermocouple, for the heating time designated by the user [7,9]. Thus, previous studies considered both thermo-electric and thermo-mechanical models (see e.g. [6,7]). In this study, the numerical modelling of the heat generated by the electrical current was carried out through an energy rate generation in the volume of the specimen, which was evaluated in each increment to assure the user-prescribed constant heating rate. For further details about the algorithm adopted see [14].

The temperature of the specimen was recorded in the experimental set-up using four thermocouples equally spaced (6 mm) along the specimen axis, as illustrated in Figure 4. The information regarding the initial and final temperature and the total time of the heating phase was extracted from the experimental data, enabling the calculation of the heating rate, which changes with the test temperature (see Table 2).

The heating phase ends when the prescribed temperature is attained at the specimen centre. Afterwards, there is a holding phase, which took 20 s in all tests performed. The use of the four thermocouples enables the extraction of the thermal gradient, along the specimen length, at the end of the holding phase, which remains approximately constant during the loading phase.

During the test, there is some heat loss by convection to the environment, which is taken into account using an air temperature of 22 °C and a convection coefficient determined as suggested in [15]. Table 2 summarizes the values determined for each test temperature. On the other hand, the

grips of the Gleeble system are in contact with the specimen and are water-cooled. In the present study, in order to simplify the model, the grips were also replaced by a convection boundary condition. Note that this convection coefficient has no physical meaning, since it must compensate also for the thermal losses due to the conduction between the specimen and the grips. Its value was determined based on the minimization of the difference between the experimentally observed and the numerically predicted thermal gradient along the specimen length, in a similar approach to the one commonly adopted to estimate the convection coefficient [6,7]. The values determined for this convection coefficient are also summarized in Table 2.

Table 2. Heating rate and convection coefficient with air and with grip (no physical meaning).

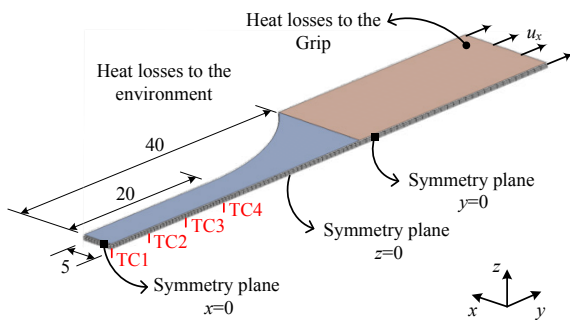| Test temperature [ºC]	Heating rate ºC/s	h_{air} [W/m²K]	h_{grip} [W/m²K]
100	3.9	15.9	30500
150	6.4	17.9	33100
200	8.9	19.5	35000

Fig. 4. Finite element model of the tensile specimen used in the Gleeble system (one eighth) with the positions of the four thermocouples TC1, TC2, TC3 and TC4.

Due to geometric and material symmetry conditions, only one eighth of the model was simulated, as shown in Figure 4. The tensile specimen was discretized using isoparametric eight-node linear hexahedral finite elements. The finite element mesh was generated in order to create nodes in the same positions of the thermocouples used in the experimental tests, to enable the analysis of the temperature gradient. The numerical simulations were all performed imposing a displacement u_x of 1.5 mm, applied as shown in Figure 4.

The elastic behaviour is assumed as isotropic and described by the Generalized Hooke law. Previous results show that the Young modulus of aluminium alloys decreases with temperature (see e.g. [12]). However, since no experimental information was available this effect was neglected. The same assumption is made for the other mechanical and thermal properties, which are summarized in Table 3. The plastic behaviour was also assumed has isotropic, described by the von Mises yield criterion.

All numerical simulations were performed with the in-house solver DD3IMP, which was originally developed to simulate isothermal sheet metal forming processes [16] and has been continuously updated to enable an improved

description of the contact conditions [17,18] and the simulation of warm forming processes. The thermo-mechanical problem is solved using the staggered coupled strategy proposed in [19].

Table 3. Mechanical and thermal characteristics of the EN AW 6061-T6 aluminium alloy.

Young modulus [MPa]	68900
Poisson's ratio	0.33
Density [kg/m³]	2700
Specificc Heat Capacity [J/kgK]	900
Thermal Conductivity [W/mK]]	167

5. Results analysis and discussion

Figure 5 compares the experimental and numerical temperature gradient along the specimen length at the end of the holding phase, showing that the simplification adopted to model the contact with the grip can lead to an accurate description of the heat losses that occur during the test. Also, it shows that the temperature difference between the centre (TC1) and TC2 increases with the test temperature, but it is always inferior to 4 ºC.
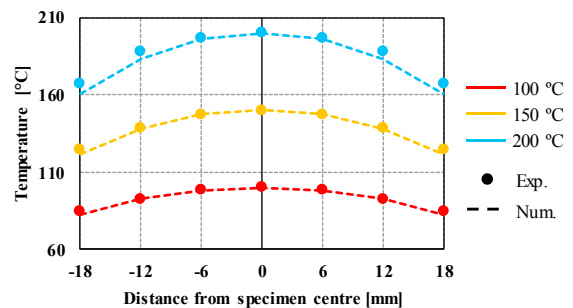

Fig. 5. Comparison between experimental and numerical temperature evolutions along the specimen length, at the end of the holding stage.

Figure 6 presents the numerically predicted evolution of the grip force with its displacement, showing that the strain rate effect is only clearly perceptible for the tests at 200 ºC, although at 150 ºC there is a very slight increase of the grip force with the increase of the strain rate. This behaviour was expected from the analysis of the parameter *m* in Eq. (2), which indicates no sensitivity to the strain rate for 150 ºC. The maximum force predicted in the experimental tests performed for the v1 strain rate is also plotted. Although not shown here, the numerical simulation at RT predicts a slightly lower (-0.3%) maximum force for a grip displacement of approximately 7.38 mm, which corresponds to an $\bar{\varepsilon}^p$ value of 0.16. For the test at 100 ºC, the numerical simulation predicts a slightly higher force (2.46%), for a grip displacement of about 4.2 mm, which corresponds to an $\bar{\varepsilon}^p$ value of 0.14. The maximum force values for the tests at 150 ºC and 200 ºC are quite well predicted, corresponding to an $\bar{\varepsilon}^p$ value of 0.12 and 0.08, respectively. The analysis of Figure 1 indicates that the values of $\bar{\varepsilon}^p$ at the maximum force are globally over predicted. Nevertheless, it should be pointed out that the numerical simulations were performed considering von Mises

isotropic behaviour, while the 6061-T6 alloy presents a normal anisotropy coefficient lower than 1 [8], whatever the test temperature. Moreover, the introduction of the temperature gradient makes it easier to deform the centre area, which always presents the higher $\bar{\varepsilon}^p$ and the force reflects the mechanical properties of this region [10].
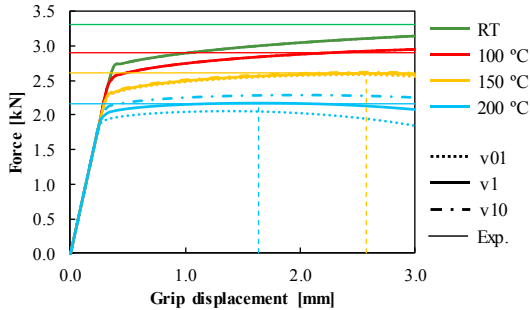

Fig. 6. Numerically predicted evolution of the grip force with its displacement and comparison with the maximum value of the experimental force for the tests performed with the intermediate strain rate. The vertical lines mark the numerically predicted onset of necking, while the horizontal lines mark the maximum force predicted in the experimental tests (only for v1 strain rate).
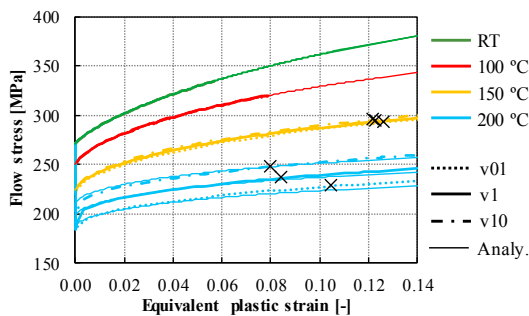

Fig. 7. Evolution of the flow stress with the plastic strain for the integration point located closer to the specimen centre and comparison with the analytical flow stress curves. The cross marks the onset of necking.

Figure 7 presents the evolution of the flow stress with the plastic strain, for the integration point located closer to the specimen centre. It is possible to observe the flow stress drop associated with the heating of the specimen, at the beginning of the test. Since the same displacement was applied to all test conditions, the maximum values attained for the plastic strain are quite different for all tests. Nevertheless, for the tests performed at RT and 100°C the values are similar, whatever the strain rate. For the tests performed at 150 °C the decrease of the strain rate leads to a slight increase of the maximum plastic strain at the centre, while for 200 °C this increase becomes quite noticeable, due to the onset of necking, which is marked in the figure with a cross. Figure 7 also includes the analytical flow curves determined by the modified Hockett-Sherby hardening law (see Eq. (1)), assuming constant values for the strain rate of 0.0002s⁻¹, 0.002 s⁻¹ and 0.02s⁻¹. This highlights that the deviation from the expected behaviour seems higher for lower strain rate values.
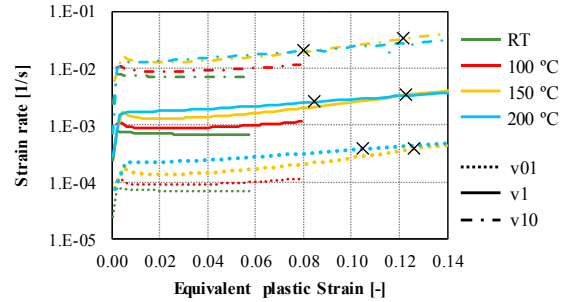

Fig. 8. Evolution of the strain rate with the equivalent plastic strain for the integration point located closer to the specimen centre. The cross marks the onset of necking.
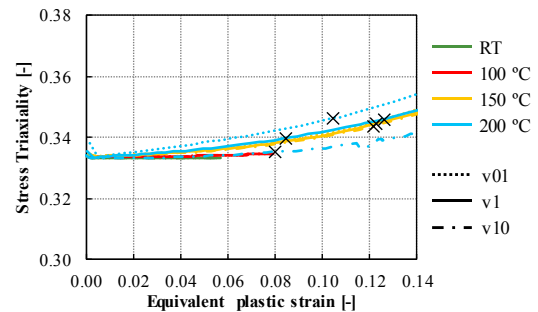

Fig. 9. Evolution of the stress triaxiality with the plastic strain for the integration point located closer to the specimen centre. The cross marks the onset of necking.

Figure 8 presents the evolution of the strain rate with the equivalent plastic strain, for the integration point located closer to the specimen centre. For the tests performed at RT, as expected there is a slight decrease of the strain rate during the test, since the grip is moving with a constant velocity and the specimen length is increasing. For the tests at 100 °C and 150 °C, there is a slight decrease in the beginning, but then it either remains almost constant (100 °C) or increases (150 °C). For 200 °C there is an increasing trend since the beginning of the deformation. These results confirm that the flow stress gradient, induced by the temperature one, alters the evolution of the strain rate at the specimen centre, during the test. In fact, the stress state is also altered, as shown in Figure 9, which presents the evolution of the stress triaxiality with the equivalent plastic strain. The uniaxial stress state is characterized by a stress triaxiality value of 1/3, which should remain constant until the onset of necking. However, the introduction of the flow stress gradient can lead to a deviation from this value, since the beginning of the deformation, which was also noticed in [5,6]. Note that the deviation is similar for all tests performed at 150 °C, while it increases faster for tests performed at lower strain rates for 200 °C. Therefore, there seems to exist a direct correlation between the flow stress gradient and the evolution of the stress triaxiality, as well as in the strain rate increase.
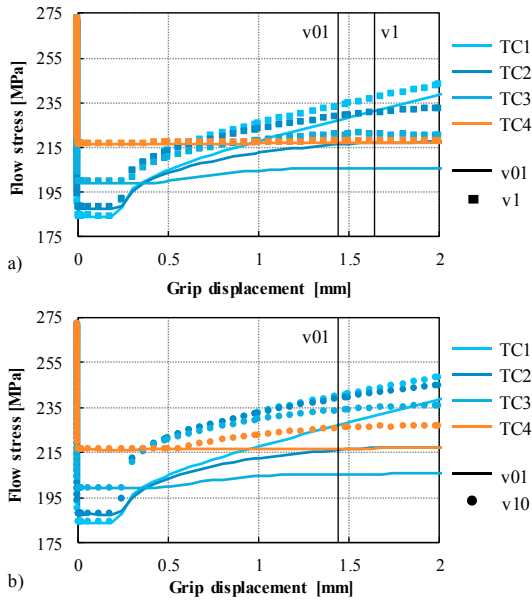
a)

b)

Fig. 10. Evolution of the flow stress with the grip displacement for the integration points located closer to TC1, TC2, TC3 and TC4. Comparison for the test at 200 ºC between: a) v01 and v1 and b) v01 and v10. The vertical line marks the onset of necking.

Figure 10 shows the evolution of the flow stress with the grip displacement for the integration points located closer to TC1, TC2, TC3 and TC4 (see Figure 4), for the tests performed at 200 ºC. Figure 10 a) compares the v01 with v1 test, while in b) the results are shown for the tests v01 and v10. The results include the heating and holding phase which correspond to a null displacement, in order to highlight the influence of the increase of temperature in the initial reduction of the flow stress, which is similar for all tests. When the grip starts to move the central point (TC1) presents the lowest flow stress, while the point located at 18mm (TC4) shows the highest. When the deformation starts to occur, the increase of the flow stress is smaller for the v01 test, since it presents the lowest strain rate and the material has a positive strain rate sensitivity. It is visible that both TC1and TC2, start to deform for the same displacement. Due to the increase of the $\bar{\varepsilon}^{\mathrm{p}}$ in TC1, even the point located at TC2 stops to deform for a grip displacement of approximately 1.44, 1.64 and 2.08 mm, for v01, v1 and v10, respectively. Moreover, for the v01 test, TC4 presents a null deformation, highlighting that this test shows a smaller deformation region. On the other hand, for the v10 test, the increase of the strain rate at the beginning of the test contributes to a more homogeneous evolution of the flow stress and a wider deformation region. This can be confirmed in Figure 11, which shows the distribution of the $\bar{\varepsilon}^{\mathrm{p}}$ for the tests at 200 ºC, at the onset of necking. This figure also shows that for lower strain rate values the distribution of the equivalent plastic strain is also less uniform along the width of the specimen, which can be related with the change in the stress path (see Figure 10).
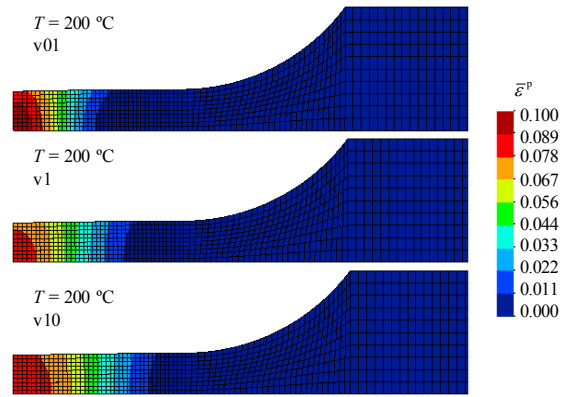

Fig. 11. Distribution of the equivalent plastic strain for the tests at 200 ºC, at the onset of necking.
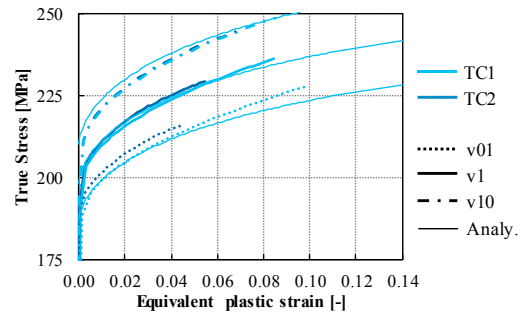

Fig. 12. Evolution of the true stress, determined using the force and the axial strain at TC1 and TC2, with the equivalent plastic strain and comparison with the analytical flow stress curves at 200°C.

Based on the knowledge of the numerical force (F) predicted until the onset of necking (see Figure 6), the true stress (σ) was evaluated using a procedure identical to the experimental one, i.e. applying the following expression:

$$\sigma = \frac{F}{A}, \text{ with } A = A_0 \exp(\varepsilon) \tag{8}$$

where A is the actual cross-sectional area, A_0 is the initial area, which in this case is equal to 10 mm², and ε is the axial strain. In this case, since the material behaviour was assumed as isotropic, the axial strain ε is identical to the equivalent plastic strain $\bar{\varepsilon}^{\mathrm{p}}$. Eq. (8) was applied using the $\bar{\varepsilon}^{\mathrm{p}}$ of the integration point located closer to TC1 and TC2 and the results are presented in Figure 12. This figure also shows the analytical flow curves calculated using the modified Hockett-Sherby hardening law, for the reference constant strain rate values. The results indicate that the use of a small gauge area for the strain analysis can help minimizing the influence of the temperature gradient on the results post-treatment. The length of this gauge area should be selected in function of the flow stress gradient induced by the temperature one.

6. Conclusions

The thermomechanical behaviour of a 6061-T6 aluminium alloy was described using a modified Hockett-Sherby hardening law, based on experimental results extracted from uniaxial tensile tests, performed in a Gleeble device. The hardening law parameters were identified using a classical approach, i.e. based on the stress-strain curves, extracted from the experimental results assuming a small length for the effective gauge area. A multi-step procedure was proposed for the parameters identification, assuming that the strain rate remains almost constant during the test. This enabled performing the numerical simulation of the uniaxial tensile tests, considering the thermomechanical behaviour of the material. In this context, a simplified numerical model that neglects the contact conditions between the specimen and the grips was proposed. Moreover, the heat generated by the electrical current is replaced by an energy rate generation in the volume of the specimen, to assure the prescribed heating rate. Therefore, this model enables the reproduction of the thermal gradient along the specimen length and due its computational efficiency can be also applied to develop inverse identification strategies for the hardening law, based on full-field measurements.

The analysis of the numerical simulation results confirms that the non-uniform temperature in the gauge area causes an heterogeneous deformation, since the regions with lower temperature deform less. For materials with positive strain rate sensitivity, the strain localization in the centre is more pronounced for higher tests temperatures and lower strain rates, since the flow stress gradient is higher. In this case, the predicted ductility is higher [7]. In such conditions, the stress state in the specimen centre can be altered since the beginning of the test, as also reported in [5]. These problems can be reduced with the improvement of grips and specimen design that enable attaining a more uniform temperature field in the gauge region [2,6]. An alternative is to resort to DIC systems to evaluate an effective gauge length that presents a uniform deformation until the onset of necking [3,10]. This enables also an improved evaluation of the evolution of the strain rate during the test. Otherwise, researchers should be aware that the hardening could be overestimated.

Acknowledgements

References

[1] Simões VM, Oliveira MC, Laurent H, Menezes LF. The punch speed influence on warm forming and springback of two Al-Mg-Si alloys. J Manuf Process 2019; 38:266–278.

[2] Ganapathy M, Li N, Lin J, Abspoel M, Bhattacharjee DA. Novel Grip Design for High-Accuracy Thermo-Mechanical Tensile Testing of Boron Steel under Hot Stamping Conditions. Exp Mech 2018; 58:243–258.

[3] Lane C, Shao Z, Zheng K, Lin J. Effect of the thickness reduction of specimens on the limit strains in thermomechanical tensile tests for hot-stamping studies. Manuf Rev 2018; 5.

[4] Abedrabbo N, Pourboghrat F, Carsley J. Forming of AA5182-O and AA5754-O at elevated temperatures using coupled thermo-mechanical finite element models. Int J Plast 2007; 23:841–875.

[5] Omer K, Butcher C, Worswick M. Characterization and application of a constitutive model for two 7000-series aluminum alloys subjected to hot forming. Int J Mech Sci 2020; 165:105218.

[6] Shao Z, Li N, Lin J, Dean TA. Strain measurement and error analysis in thermo-mechanical tensile tests of sheet metals for hot stamping applications. Proc Inst Mech Eng Part C: J Mech Eng Sci 2018; 232:1994–2008.

[7] Kardoulaki E, Lin J, Balint D, Farrugia D. Investigation of the effects of thermal gradients present in Gleeble high-temperature tensile tests on the strain state for free cutting steel. J Strain Anal Eng Des 2014; 49:521–532.

[8] Simões VM, Laurent H, Oliveira MC, Menezes LF. The influence of warm forming in natural aging and springback of Al-Mg-Si alloys. Int J Mater Form 2019; 12:57–68.

[9] Coër J, Bernard C, Laurent H, Andrade-Campos A, Thuillier S. The Effect of Temperature on Anisotropy Properties of an Aluminium Alloy. Exp Mech 2011; 51:1185–1195.

[10] Wang Z, Zang S, Chu X, Zhang S, Lionel L. Identification of 7B04 aluminum alloy anisotropy yield criteria with conventional test and Pottier test at elevated temperature. Results Phys 2019; 15:102655.

[11] Wagoner RH, Nakamachi E, Germain Y. Analysis of sheet forming operations using the finite element method. In: Proceedings of the IDDRG working groups; 1988.

[12] Laurent H, Coër J, Manach P.Y, Oliveira M.C, Menezes L.F. Experimental and numerical studies on the warm deep drawing of an Al–Mg alloy. Int J Mech Sci 2015; 93:59–72.

[13] Andrade-Campos A, De-Carvalho R, Valente RAF. Novel criteria for determination of material model parameters. Int J Mech Sci 2012; 54:294–305.

[14] Martins JMP, Alves JL, Neto DM, Oliveira MC, Menezes LF. Numerical analysis of different heating systems for warm sheet metal forming. Int J Adv Manuf Technol 2016; 83:897-909.

[15] Bergman TL, Lavine AS, Incropera FP, Dewitt DP. Fundamentals of Heat and Mass Transfer. 7th ed. John Wiley & Sons; 2011.

[16] Menezes LF, Teodosiu C. Three-dimensional numerical simulation of the deep-drawing process using solid finite elements. J Mater Process Technol 2000; 97:100–106.

[17] Oliveira MC, Alves JL, Menezes LF. Algorithms and strategies for treatment of large deformation frictional contact in the numerical simulation of deep drawing process. Arch Comput Methods Eng 2008; 15:113-162.

[18] Neto DM, Oliveira MC, Menezes LF. Surface Smoothing Procedures in Computational Contact Mechanics. Arch Comput Methods Eng 2015; 24:37–87.

[19] Martins JMP, Neto DM, Alves JL, Oliveira MC, Laurent H, Andrade-Campos A, Menezes LF. A new staggered algorithm for thermomechanical coupled problems. Int J Solids Struct 2017; 122–123:42-58.